A Transient Vanadium Flow Battery Model Incorporating Vanadium Crossover and Water Transport through the Membrane

K. W. Knehr, Ertan Agar, C. R. Dennison, A. R. Kalidindi and E. C. Kumbur

Email alerting service	Receive free email alerts when new articles cite this article - sign up in the box at the top right corner of the article or click here

A Transient Vanadium Flow Battery Model Incorporating Vanadium Crossover and Water Transport through the Membrane

K. W. Knehr,* Ertan Agar,* C. R. Dennison,* A. R. Kalidindi, and E. C. Kumbur**,z

Electrochemical Energy Systems Laboratory, Department of Mechanical Engineering and Mechanics, Drexel University, Philadelphia, Pennsylvania 19104, USA
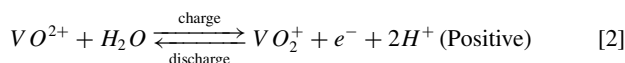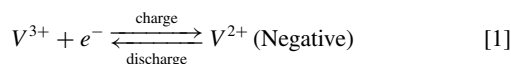
This paper presents a 2-D transient, isothermal model of a vanadium redox flow battery that can predict the species crossover and related capacity loss during operation. The model incorporates the species transport across the membrane due to convection, diffusion, and migration, and accounts for the transfer of water between the half-cells to capture the change in electrolyte volume. The model also accounts for the side reactions and associated changes in species concentration in each half-cell due to vanadium crossover. A set of boundary conditions based on the conservations of flux and current are incorporated at the electrolyte|membrane interfaces to account for the steep gradients in concentration and potential at these interfaces. In addition, the present model further improves upon the accuracy of existing models by incorporating a more complete version of the Nernst equation, which enables accurate prediction of the cell potential without the use of a fitting voltage. A direct comparison of the model predictions with experimental data shows that the model accurately predicts the measured voltage of a single charge/discharge cycle with an average error of 1.83%, and estimates the capacity loss of a 45 cycle experiment with an average error of 4.2%.
© 2012 The Electrochemical Society. [DOI: 10.1149/2.017209jes] All rights reserved.

The vanadium redox flow battery (VRFB) is an emerging energy storage technology that offers unique solutions for smart grid applications, such as renewable energy storage, peak shaving, and electric utility load leveling. In these systems, liquid electrolytes are stored in external tanks and circulated through a cell stack, where the energy conversion process occurs due to electrochemical reduction-oxidation reactions. These reactions occur on porous graphite felt electrodes which are separated by an ion exchange membrane. The role of the membrane is to keep the solutions separate while allowing for the transfer of H+ protons to maintain electroneutrality in the electrolytes. The key advantage of the VRFB is the that energy storage and power generation are decoupled, such that the energy storage capacity is determined by the volume of the external tanks, and the power rating is determined by the geometry and number of the electrochemical cells.

Among the flow battery types, the VRFB distinguishes itself by using different oxidation states of the same vanadium element in the redox reactions.[1] During charge/discharge of a VRFB, the redox reactions occur simultaneously in both half-cells as follows:

$$V^{3+} + e^- \underset{\text{discharge}}{\overset{\text{charge}}{\rightleftarrows}} V^{2+} \text{ (Negative)} \quad [1]$$

$$VO^{2+} + H_2O \underset{\text{discharge}}{\overset{\text{charge}}{\rightleftarrows}} VO_2^+ + e^- + 2H^+ \text{ (Positive)} \quad [2]$$

where VO^{2+} and VO_2^+ represent vanadium in the V(IV) and V(V) oxidation states, respectively. The utilization of the same, but differently charged liquid electrolytes eliminates the problem of electrolyte cross-contamination because, unlike other redox couples, the mixing of the electrolytes does not result in irreversible side reactions and poisoning of the electrolytes. Other advantages of VRFBs include high efficiency (up to 85%), long charge/discharge cycle life, and full discharge capability.[2–4]

Currently, the long-term performance of these systems is limited by the significant loss of available stored energy (i.e., capacity loss) in the electrolytes over time.[5] The capacity loss occurs primarily due to the undesired transport of active vanadium species across the membrane, which is known as crossover.[5] Along with reducing capacity, vanadium crossover also initiates reversible side reactions in the electrolytes, which decrease the coulombic efficiency during cycling. To date, membrane research in this field has mainly focused on the development of chemically stable membrane materials that reduce the

permeability of vanadium ions (to minimize crossover) while maintaining high ionic conductivity of hydrogen protons to minimize the ohmic losses.[6–10]

Due to the high cost and lengthy time requirements of experimental studies, performance studies have been conducted through the development of mathematical models. Only a very few (less than fifteen) modeling studies[11–22] have been reported so far. In general, these models are based on the approaches adopted from PEM fuel cell literature due to the similarity of these systems, and are primarily focused on understanding the system behavior and identifying the major losses in VRFBs. A good review of the modeling efforts is provided in.[23]

The first model for VRFB systems was introduced by Li and Hikihara.[11] They developed a zero-dimensional, transient model that simulates the mechanical (pumping) and electrochemical performance of a VRFB system.[11] Soon after, Shah et al.[12] developed a transient, two-dimensional model of a single cell, which was used to predict the temporal distributions of the reactants and analyze the effects of inlet flow rates on VRFB performance. In other work by the same group, this model was expanded to include the effects of heat generation, localized temperature variations, and hydrogen/oxygen evolution.[13–15] You et al.[16] later utilized the mathematical framework developed by Shah et al.[12] to formulate a steady state model in order to predict the effects of applied current density and state-of-charge (SOC) on the performance. Vynnycky[17] proposed scaling and asymptotic methods to reduce the complexity of the model developed by Shah et al.[12] for analysis of large-scale VRFB stacks. Recently, Ma et al.[18] have utilized the same framework to develop a 3D model of a negative electrode to study the effects of electrolyte velocity on VRFB performance.

While these pioneering studies provide useful tools for rapid analysis of VRFB operation, they are based on some assumptions which may hinder their ability to predict all the physical and chemical phenomena that take place in these systems. For instance, one limitation in these models is the inaccuracy of the predicted cell voltage. A constant fitting voltage of 131 to 140 mV (~10% of the total voltage) is typically added to the predicted voltage in order to account for unknown discrepancies with experimental data. In a previous work by the authors,[24] it was suggested that this discrepancy is caused by the utilization of an incomplete version of the Nernst equation when calculating the maximum theoretical voltage – open circuit voltage (OCV) – of the system. To address this issue, a more complete version of the Nernst equation that accounts for the proton activity at the positive electrode and the Donnan potential across the membrane was proposed to provide a better means for predicting the OCV.[24]

Another limiting assumption in these models is that they treat the membrane as a perfectly selective membrane which allows for the transport of *only* hydrogen protons; such that vanadium ions and

*Electrochemical Society Student Member.
**Electrochemical Society Active Member.
zE-mail: eck32@drexel.edu

negatively charged species are not permitted to transport through the membrane. However, in reality, the ion-exchange membranes used in these systems are not ideally perm-selective. Therefore, both negatively and positively charged species are able to transport through the membrane, which results in side reactions and capacity loss.[25]

Recently, Skyllas-Kazacos and her co-workers[20,21] developed a zero-dimensional model which simulates the capacity loss of a static VRFB cell during cycling. The model was used to predict trends in capacity loss as a result of gas evolution and side reactions caused by the diffusion of vanadium through the membrane. While this model provides a useful starting point for the simulation of crossover during VRFB operation, it accounts for *only* the diffusion of vanadium ions through the membrane, and does not include the other species (e.g., water, bisulfate and hydrogen ions) and the other ion transport mechanisms (e.g., migration and convection). A good extension of this model would be to incorporate all three mechanisms of species transport (e.g., migration, convection and diffusion), the transport of all species through the membrane, and the interfacial mass transport at the electrolyte|membrane interface, which is essential to accurately couple the species crossover in the membrane with the mass transport in the electrodes.

Here, we present a 2-D, transient, isothermal model which incorporates the transport of all species (i.e., vanadium, water, hydrogen ions and bisulfate) through the membrane and accounts for the changes in the membrane potential due to the species concentrations and the semi-permselective nature of the membrane. In particular, the model incorporates all three modes of species transport across the membrane (i.e., convection, diffusion, and migration) and accounts for the transfer of water between the half-cells and the side reactions associated with the species crossover. It also utilizes a set of boundary conditions based on the conservations of flux and current at the electrolyte|membrane interfaces to account for the steep gradients in concentration and potential at these interfaces. Finally, the present model accounts for the contribution of the proton activity on the OCV at the positive electrode, which enables accurate prediction of the cell potential without the use of a fitting voltage. In the following sections, the formulation of the model is presented along with a detailed discussion of the model capabilities and an analysis of the charge/discharge simulations performed by the model.

Method of Approach

Modeling.— The present model consists of five domains, namely: the current collectors, the porous positive electrode, the porous negative electrode and the membrane (Fig. 1). The model is constructed based on the following assumptions:

Figure 1. Schematic of the VRFB system and modeling domains.

1. All domains in the cell are considered isothermal.
2. Electrolyte flow is incompressible.
3. The mass and charge transfer properties of the electrode, electrolyte and membrane (i.e., resistivity, viscosity, diffusion coefficients, etc.) are assumed to be isotropic.
4. Hydrogen and oxygen evolution reactions are neglected.
5. The dilute solution approximation is utilized for species transport.
6. Variations in concentration, potential, and pressure in the z-direction are neglected.

Porous Electrode.—In each half-cell, liquid electrolytes consisting of water, sulfuric acid (i.e., H^+, HSO_4^-, and SO_4^{2-}) and charged vanadium species (i.e., V^{2+}, V^{3+}, VO^{2+}, and VO_2^+) flow through the porous carbon electrodes. The conservation of mass for each charged species is defined using the following equation:

$$\frac{\partial}{\partial t}\left(\varepsilon c_i^e\right) + \nabla \cdot \vec{N}_i^e = -S_i \quad [3]$$

where c_i^e is the bulk concentration of species i in the electrolyte (e), ε is the porosity of the electrode, $\vec{N}_i^e$ is the flux of the charged species in the electrolyte, and S_i denotes the source term for the species. Equation 3 applies to all charged species except SO_4^{2-}, which is calculated from the condition of electroneutrality in the electrolyte as shown below:

$$\sum_i z_i c_i^e = 0 \quad [4]$$

where z_i is the valence for species i.

In Eq. 3, the source term S_i (given in Table I) represents the change in concentration of species i due to the electrochemical reactions in the half cells and the dissociation of H_2SO_4 (Eq. 5). It is important to note that since the electrolytes contain less than the experimentally observed limit of H_2SO_4 (40 mol kg^{-1} [26]), it is safe to assume that the first step of dissociation ($H_2SO_4 \rightarrow H^+ + HSO_4^-$) is fully complete. The second step of dissociation ($HSO_4^- \rightarrow H^+ + SO_4^{2-}$) can be described using a dissociation source term (S_d), which represents the changes in the concentrations of the species in order to maintain the correct ionic ratios, and is given as follows:

$$S_d = k_d\left(\frac{c_{H^+}^e - c_{HSO_4^-}^e}{c_{H^+}^e + c_{HSO_4^-}^e} - \beta\right) \quad [5]$$

where β is the degree of dissociation of HSO_4^-, which is determined experimentally[26] and is assumed to be constant in this study. The term k_d represents the dissociation reaction coefficient, which is used as a fitting parameter to model instantaneous dissociation of the acid.

The flux of each species in Eq. 3 is defined by the Nernst-Planck equation, which determines species movement due to diffusion, migration, and convection:

$$\vec{N}_i^e = -D_i^{eff}\nabla c_i^e - z_i u_i^e c_i^e F \nabla \phi_l^e + \vec{v}_j c_i^e \quad [6]$$

where ϕ_l^e is the ionic (liquid) potential, μ_i^e is the ionic mobility and $\vec{v}_j$ is the velocity of the electrolyte j. The term D_i^{eff} represents the effective diffusion coefficient, which is calculated using the Bruggemann correlation (Eq. 7).

$$D_i^{eff} = \varepsilon^{3/2} D_i \quad [7]$$

Under the dilute solution approximation, the ionic mobility in the electrolyte, u_i^e (see Eq. 6) is represented using the Nernst-Einstein equation, which is given as follows:[27]

$$u_i^e = \frac{D_i^{eff}}{RT} \quad [8]$$

where R is the universal gas constant and T is temperature.

The bulk velocity ($\vec{v}_j$) can be determined using the following continuity equation:

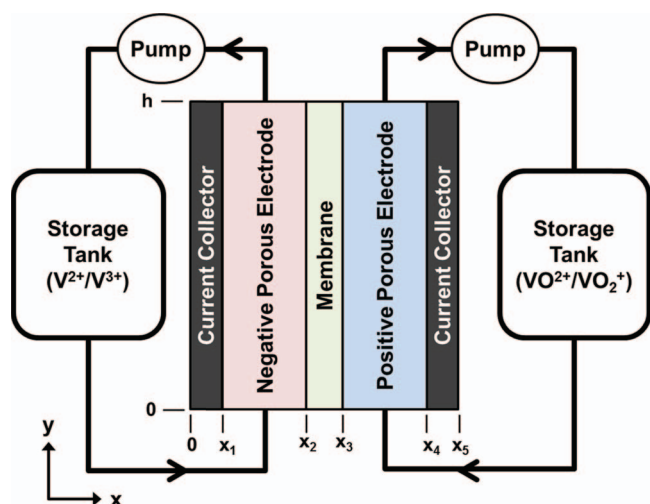$$\nabla \cdot (\rho_j \vec{v}_j) = S_{m,j} \quad [9]$$

Table I. Mass, dissociation, and reaction source terms.

Term	Description	Positive electrode	Negative electrode
S_{II}	V(II) concentration equation (mol m^{-3})	—	i/F
S_{III}	V(III) concentration equation (mol m^{-3})	—	$-i/F$
S_{IV}	V(IV) concentration equation (mol m^{-3})	i/F	—
S_V	V(V) concentration equation (mol m^{-3})	$-i/F$	—
S_{H^+}	Proton concentration equation (mol m^{-3})	$-S_d$	$-2i/F - S_d$
$S_{HSO_4^-}$	Bisulfate concentration equation (mol m^{-3})	S_d	S_d
S_m	Velocity continuity equation (kg m^{-3} s^{-1})	$\frac{i \cdot M_w}{F \cdot w_{cell}}$	0

where ρ_j is the density of electrolyte j. The term $S_{m,j}$ represents the mass source term which describes the generation or depletion of water in the cell due to the electrochemical reactions and is given in Table I. To account for variations in electrolyte volume, water is treated as a volume instead of a concentrated species in the model formulation. The velocity term ($\vec{v}_j$) in Eq. 9 is calculated using Darcy's law:

$$\vec{v}_j = -\frac{\kappa}{\mu_j} \nabla p_j \tag{10}$$

where, μ_j is the dynamic viscosity of the electrolyte, p_j is the pressure, and κ is the effective permeability of the electrode, which is determined using the Kozeny-Carman equation:

$$\kappa = \frac{4r_p^2}{C_{KC}} \frac{\varepsilon^3}{(1-\varepsilon)^2} \tag{11}$$

The term r_p in Eq. 11 represents the mean radius of the electrode pores, and C_{KC} is the Kozeny-Carman constant.[28] Due to the lack of data regarding the electrolyte viscosity of a VRFB, a constant value of μ_j is used for each electrolyte, which represents the viscosity of the electrolyte at 50% state of charge (SOC).[29] The values of μ_j and the other electrolyte properties are listed in Table II.

The species transport, electrochemical reactions, and current in the electrode domain are coupled through the conservation of charge:

$$\nabla \cdot \vec{j}_l^e = -\nabla \cdot \vec{j}_s^e = i \tag{12}$$

Table II. Electrolyte properties and parameters.

Symbol	Description	Value
k_d	HSO$_4^-$ dissociation reaction rate constant (s^{-1})[a]	1×10^4
β	HSO$_4^-$ degree of dissociation	0.25[26]
μ_-	Average dynamic viscosity of negative electrolyte (Pa s)	0.0025[29]
μ_+	Average dynamic viscosity of positive electrolyte (Pa s)	0.005[29]
ρ_-	Average density of negative electrolyte (kg m^{-3})	1300[29]
ρ_+	Average density of positive electrolyte (kg m^{-3})	1350[40]
ρ_w	Density of water (kg m^{-3})	999[41]
D_{II}	V(II) diffusion coefficient (m^2 s^{-1})	2.4×10^{-10} [42]
D_{III}	V(III) diffusion coefficient (m^2 s^{-1})	2.4×10^{-10} [42]
D_{IV}	V(IV) diffusion coefficient (m^2 s^{-1})	3.9×10^{-10} [42]
D_V	V(V) diffusion coefficient (m^2 s^{-1})	$3..9 \times 10^{-10}$ [42]
D_{H^+}	H$^+$ diffusion coefficient (m^2 s^{-1})	9.312×10^{-9} [31]
$D_{HSO_4^-}$	HSO$_4^-$ diffusion coefficient (m^2 s^{-1})	1.33×10^{-9} [31]
$D_{SO_4^{2-}}$	SO$_4{}^{2-}$ diffusion coefficient (m^2 s^{-1})	1.065×10^{-9} [31]

[a]Fitted parameter

where i is the reaction current density. $\vec{j}_l^e$ and $\vec{j}_s^e$ denote the liquid (ionic) and solid (electronic) current density in the electrode domain, respectively, and are given as follows:

$$\vec{j}_l^e = F \sum_i z_i \vec{N}_i^e \tag{13a}$$

$$\vec{j}_s^e = \sigma_s^e \nabla \phi_s^e \tag{13b}$$

where σ_s^e is the bulk conductivity of the electrode, and its value is given in Table III along with the other properties of the electrodes and current collectors.

The local reaction current density (i) is expressed by the Butler-Volmer equations, which are given in Eq. (14) for both the negative ('−') and positive ('+') electrodes.

$$i_- = aFk_- \left(c_{II}^e\right)^{(1-\alpha_-)} \left(c_{III}^e\right)^{\alpha_-} \left[\left(\frac{c_{II}^s}{c_{II}^e}\right) \exp\left(\frac{(1-\alpha_-)F\eta_-}{RT}\right) \right.$$
$$\left. - \left(\frac{c_{III}^s}{c_{III}^e}\right) \exp\left(\frac{-\alpha_- F\eta_-}{RT}\right)\right] \tag{14a}$$

$$i_+ = aFk_+ \left(c_{IV}^e\right)^{(1-\alpha_+)} \left(c_V^e\right)^{\alpha_+} \left[\left(\frac{c_{IV}^s}{c_{IV}^e}\right) \exp\left(\frac{(1-\alpha_+)F\eta_+}{RT}\right) \right.$$
$$\left. - \left(\frac{c_V^s}{c_V^e}\right) \exp\left(\frac{-\alpha_+ F\eta_+}{RT}\right)\right] \tag{14b}$$

In Eq. (14), k represents the reaction rate constant, and α denotes the charge transfer coefficient. The term a is the specific surface area of the porous electrode, whereas η represents the overpotential and is defined as follows:

$$\eta_j = \phi_l^e - \phi_s^e - E_{0,j} \tag{15}$$

Table III. Electrode and current collector properties.

Symbol	Description	Value
ε	Electrode porosity[a]	0.93
r_p	Mean pore radius (μm)[a]	50.3
a	Specific surface area (m^{-1})[a]	3.5×10^4
C_{KC}	Kozeny-Carmen Coefficient	180[28]
h_{cell}	Electrode height (m)	0.035
w_{cell}	Electrode width (m)	0.0285
L^e	Electrode thickness (m)	0.004
L^{cc}	Current collector thickness (m)	0.06
σ_s^e	Electronic conductivity of electrode (S m^{-1})[b]	66.7
σ_s^{cc}	Electronic conductivity of current collector (S m^{-1})[c]	1000

[a]Experimentally determined (Section 2.1.1)
[b]Supplied by Manufacturer (SGL Carbon Group, Germany)
[c]Estimated

Table IV. Kinetic parameters.

Symbol	Description	Value
k_-	Reaction rate constant for negative reaction (m s^{-1})[a]	7.0×10^{-8}
k_+	Reaction rate constant for positive reaction (m s^{-1})[a]	2.5×10^{-8}
α_-	Negative charge transfer coefficient[a]	0.45
α_+	Positive charge transfer coefficient[a]	0.55
$E'_{0,-}$	Standard reduction potential at negative electrode (V)	-0.255[12]
$E'_{0,+}$	Standard reduction potential at positive electrode (V)	1.004[12]

[a]Fitted

where $E_{0,j}$ represents the open circuit voltage (OCV) of each half-cell calculated using the Nernst equations given as follows:

$$E_{0,-} = E'_{0,-} + \frac{RT}{F} \ln \left(\frac{c^e_{III}}{c^e_{II}} \right) \text{ (Negative)} \quad [16a]$$

$$E_{0,+} = E'_{0,+} + \frac{RT}{F} \ln \left(\frac{c^e_V \cdot (c^e_{+,H^+})^2}{c^e_{IV}} \right) \text{ (Positive)} \quad [16b]$$

In Eq. (16), $E'_{0,-}$ and $E'_{0,+}$ represent the standard reduction potentials for the negative and positive electrodes, respectively. In the presence of an electric field, like the Galvani potentials of a VRFB, ionic bonds become stretched and weakened, leading to an increase in the dissociation of the ions. Therefore, when determining c^e_{+,H^+} in Eq. 16b, all protons initially bonded to SO_4^{2-} are assumed to be fully dissociated, existing as free protons.[24] The input parameters describing the reaction kinetics in Eqs. (14)–(16) are listed in Table IV.

In the Bulter-Volmer equations (Eq. (14)), c^s_i denotes the surface concentration of species i at the liquid-solid interface of the electrode. For the negative half-cell, these concentrations are determined by solving for c^s_{II} and c^s_{III} in the following equations:[12]

$$F D_{II} \left(\frac{c^e_{II} - c^s_{II}}{r_p} \right) = F k_- \left(c^e_{II} \right)^{(1-\alpha_-)} \left(c^e_{III} \right)^{\alpha_-}$$
$$\times \left[\left(\frac{c^s_{II}}{c^e_{II}} \right) \exp \left(\frac{(1-\alpha_-)F\eta_-}{RT} \right) \right.$$
$$\left. - \left(\frac{c^s_{III}}{c^e_{III}} \right) \exp \left(\frac{-\alpha_- F\eta_-}{RT} \right) \right] \quad [17a]$$

$$F D_{III} \left(\frac{c^e_{III} - c^s_{III}}{r_p} \right) = F k_- \left(c^e_{II} \right)^{(1-\alpha_-)} \left(c^e_{III} \right)^{\alpha_-}$$
$$\times \left[\left(\frac{c^s_{III}}{c^e_{III}} \right) \exp \left(\frac{-\alpha_- F\eta_-}{RT} \right) \right.$$
$$\left. - \left(\frac{c^s_{II}}{c^e_{II}} \right) \exp \left(\frac{(1-\alpha_-)F\eta_-}{RT} \right) \right] \quad [17b]$$

where r_p (the mean pore radius of the electrode) represents the average diffusive path-length. In the positive half-cell, c^s_{IV} and c^s_V can be determined by developing a similar system of equations using Eq. 14b. For brevity, these equations are not included in this paper, but a detailed description of this formulation can be found in.[12–15]

Current Collector.—The current collectors are composed of impermeable solid graphite. Therefore, all current within this domain is electronic and governed by Ohm's law:

$$\vec{j}^{cc}_s = -\sigma^{cc}_s \nabla \phi^{cc}_s \quad [18]$$

where σ^{cc}_s is the conductivity of the current collector.

Membrane.—Unlike previous models, the present model accounts for the transport of all charged species through the membrane, including: V^{2+}, V^{3+}, VO^{2+}, VO_2^+, H^+, and HSO_4^-. Each of the positive species (i.e., vanadium and protons) satisfies the following mass balance:

$$\frac{\partial c^m_i}{\partial t} = -\nabla \cdot \vec{N}^m_i \quad [19]$$

where c^m_i represents the concentration of species i in the membrane (m), and the flux, $\vec{N}^m_i$, is defined using the Nernst-Planck equation (Eq. 6). The concentration of the bisulfate, HSO_4^-, is calculated from the condition of electroneutrality in the membrane as shown below:

$$z_f c_f + \sum_i z_i c^m_i = 0 \quad [20]$$

where z_f and c_f represent the charge and concentration of the fixed sulfonic acid groups that are present in the ion-exchange membrane (e.g., Nafion), respectively. It is important to note that SO_4^{2-} is not present in the membrane because it is assumed that the dissociation of HSO_4^- is completely suppressed by the presence of the fixed charge in the membrane.[30]

For the Nernst-Planck equation (Eq. 6) in the membrane, the velocity ($\vec{v}^m$) is given by an alternate form of Schlogl's equation:[25]

$$\vec{v}^m = -\frac{\kappa_p}{\mu_w} \nabla p - \frac{\kappa_\phi}{\mu_w} c_f F \left(\nabla \phi^m_l + \nabla \phi^m_{diff} \right) \quad [21]$$

where μ_w is the viscosity of water, κ_ϕ is the electrokinetic permeability and κ_p is the hydraulic permeability. The first term represents the osmosis of water through the membrane as a result of pressure differences between the half-cells. The second term represents the electro-osmotic convection caused by the viscous interactions between the fluid and the mobile ions, where $F(\nabla \phi^m_l + \nabla \phi^m_{diff})$ represents the body force acting on the mobile ions. The term $\nabla \phi^m_l$ accounts for the liquid potential difference across the membrane, and $\nabla \phi^m_{diff}$ is the effective diffusion potential, which accounts for the viscous drag as a result of ion diffusion and is calculated as follows:[31]

$$\nabla \phi^m_{diff} = \frac{F \sum_i z_i D^m_i \nabla c^m_i}{\sigma^m_{eff}} \quad [22]$$

where σ^m_{eff} is the effective conductivity of the membrane:

$$\sigma^m_{eff} = \frac{F^2}{RT} \sum_i z_i^2 D^m_i c^m_i \quad [23]$$

In the membrane, only ionic current exists ($\nabla \vec{j}_l = 0$) and similar to the porous electrode, it is proportional to the flux of all the species and is calculated using Eq. 13a ($\vec{j}^m_l = F \sum_i z_i \vec{N}^m_i$). The properties used for the membrane are provided in Table V.

Membrane|Electrolyte Interface.—At the membrane|electrolyte interface, current and species flux are continuous; however, the potential and species concentrations are *discontinuous* due to the permselective nature of the membrane.[25] In order to simulate this interfacial region and account for these discontinuities, the membrane|electrolyte interface is modeled as a region with finite thickness. A set of boundary conditions have been developed to describe the mass transport at the interface, and the derivation of these equations is explained below.

The membrane|electrolyte interface is composed of a membrane region with a thickness of δ^m and an electrolyte region with a thickness of δ^e. When compared, the membrane|electrolyte interface in a VRFB resembles the interface that can be seen at the surface of a flow-by electrode, where a flow-by electrode is defined as an electrode with a liquid electrolyte flowing over its surface (e.g., those found in electrochemical cells where the liquid is displaced due to stirring or pumping, e.g., a rotating disk electrode). Therefore, it is reasonable to assume that δ^e is equivalent to the diffusion boundary layer that exists at the surface of a flow-by electrode, where the thickness of this layer

Table V. Membrane properties and parameters.

Symbol	Description	Value
L^m	Membrane thickness (μm)	203[43]
c_f	Fixed acid concentration (mol m^{-3})	1990[43]
z_f	Fixed acid charge	−1
κ_ϕ	Electrokinetic permeability (m^2)[a]	1.13×10^{-20}
κ_p	Hydraulic permeability (m^2)	1.58×10^{-18} [44]
K_ϕ	Interfacial potential fitting parameter[a]	0.25
D_{II}^m	V(II) membrane diffusion coefficient (m^2 s^{-1})[a]	3.125×10^{-12}
D_{III}^m	V(III) membrane diffusion coefficient (m^2 s^{-1})	5.93×10^{-12} [45]
D_{IV}^m	V(IV) membrane diffusion coefficient (m^2 s^{-1})	5.0×10^{-12} [45]
D_V^m	V(V) membrane diffusion coefficient (m^2 s^{-1})	1.17×10^{-12} [45]
$D_{H^+}^m$	H$^+$ membrane diffusion coefficient (m^2 s^{-1})	3.35×10^{-9} [30]
$D_{HSO_4^-}^m$	HSO$_4^-$ membrane diffusion coefficient (m^2 s^{-1})	4×10^{-11} [46]

[a]Fitted parameter

can be calculated as follows:[32]

$$\delta^e = \delta_{momentum} \left(\frac{D_{avg}^{eff} \rho_j}{\mu_j} \right)^{1/3} \qquad [24]$$

In Eq. 24, D_{avg}^{eff} represents the average effective diffusion coefficient of the species, and $\delta_{momentum}$ is the thickness of the hydrodynamic momentum boundary layer (Fig. 2), which is the zone next to the electrode where the velocity changes from zero to the bulk velocity. The value of $\delta_{momentum}$ can be determined for a fully developed laminar flow through a porous media (in this case, the electrode) in contact with a flat plate (in this case, rigid polymer membrane) as follows:[33]

$$\delta_{momentum} = \sqrt{\frac{\kappa}{\varepsilon}} \qquad [25]$$

In terms of the thickness of the membrane region at the interface (δ^m), to the best of our knowledge, there is no established theoretical method for calculating δ^m. In the present model, we assume that δ^m is equivalent to δ^e for simplicity. Since δ^e is typically less than 1% of the membrane thickness (~200 μm), it is reasonable to assume linear variations in concentration and potential over these small regions. Furthermore, because the steep concentration and potential gradients at the interfa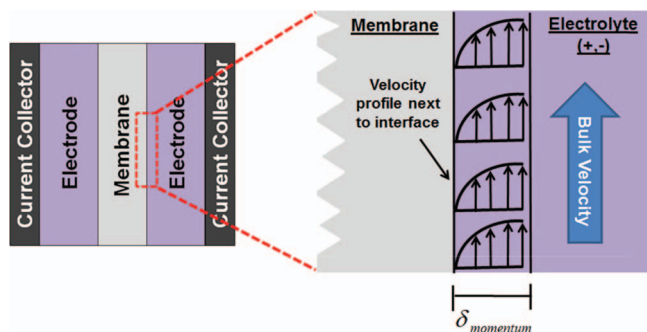ce cause large diffusion and migration fluxes, the contribution of convection to the total species flux can be assumed negligible. Using these two assumptions, one can determine the flux of each species in the electrolyte (δ^e) and membrane (δ^m) regions at the membrane|electrolyte interface by discretizing the diffusion and migration terms in the Nernst-Plank equation (Eq. 6) as follows:

$$N_i^{er} = -D_i^{eff} \frac{\left(c_i^e - c_i^{junc} \right)}{\delta^e} - z_i u_i^e F \frac{\left(c_i^e + c_i^{junc} \right)}{2} \frac{K_\phi \left(\phi_l^e - \phi_l^m \right)}{\delta^e} \qquad [26a]$$

$$N_i^{mr} = -D_i^m \frac{\left(c_i^{junc} - c_i^m \right)}{\delta^m} - z_i u_i^m F \frac{\left(c_i^{junc} + c_i^m \right)}{2}$$
$$\times \frac{(1 - K_\phi) \left(\phi_l^e - \phi_l^m \right)}{\delta^m} \qquad [26b]$$

where N_i^{er} and N_i^{mr} are the fluxes of species i in the electrolyte interface region and membrane interface region, respectively. The term c_i^{junc} represents the concentration of species i at the membrane|electrolyte junction (Fig. 3a), and K_ϕ is a fitting parameter that represents the percentage of the total potential jump ($\phi_l^e - \phi_l^m$) occurring in the electrolyte interface region (Fig. 3c).

The concentration of each species at the membrane|electrolyte interface (c_i^{junc}) can be calculated by setting the fluxes at the interface equal ($N_i^{er} = N_i^{mr}$) and solving for c_i^{junc}. This procedure is valid for all membrane species except HSO$_4^-$, which is assumed to be discontinuous at the junction due to the fixed charge in the membrane. In order for the electrolyte and membrane regions to remain electrically neutral, the HSO$_4^-$ concentration at the junction must satisfy the following condition of electroneutrality (Fig. 3b):
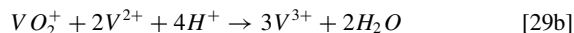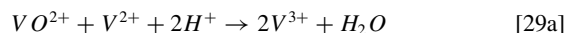
$$c_{HSO_4^-}^{junc,m} = c_{HSO_4^-}^{junc,e} - c_f \qquad [27]$$

The concentration of the bisulfate at the electrolyte side of the interface ($c_{HSO_4^-}^{junc,e}$) can be calculated by *i*) replacing the term c_i^{junc} in Eqs. 26a and 26b with $c_{HSO_4^-}^{junc,e}$ and ($c_{HSO_4^-}^{junc,e} - c_f$), respectively, *ii*) setting the fluxes at the interface equal ($N_{HSO_4^-}^{er} = N_{HSO_4^-}^{mr}$), and *iii*) solving for $c_{HSO_4^-}^{junc,e}$.

Using the equations developed for the species flux, the membrane interfacial region can be incorporated into the model by applying the following boundary condition on the charged species at the membrane|electrolyte interface:
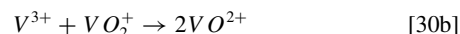
$$-\vec{n} \cdot \vec{N}_i^m = -N_i^{mr} \quad \text{at x} = \text{x}_2 \text{ and x} = \text{x}_3 \qquad [28]$$

where $\vec{n}$ denotes the outward normal unit vector and x$_2$ and x$_3$ refer to the membrane|electrolyte interface at the '−' and '+' half-cells, respectively (see Fig. 1). At the electrolyte interfacial region, the side reactions due to crossover must be incorporated into the boundary conditions. It is reported that the vanadium crossover through the membrane will result in the following side reactions in the electrolytes:[5]

Negative electrolyte:

$$VO^{2+} + V^{2+} + 2H^+ \rightarrow 2V^{3+} + H_2O \qquad [29a]$$

$$VO_2^+ + 2V^{2+} + 4H^+ \rightarrow 3V^{3+} + 2H_2O \qquad [29b]$$

Positive electrolyte:

$$V^{2+} + 2VO_2^+ + 2H^+ \rightarrow 3VO^{2+} + H_2O \qquad [30a]$$

$$V^{3+} + VO_2^+ \rightarrow 2VO^{2+} \qquad [30b]$$

These reactions were observed during a self-discharge study with no net current exchange between the graphite felt electrodes and electrolyte. Therefore, it is safe to assume that these reactions are chemical in nature (as opposed to electrochemical) and are not hindered by the slow kinetics of the un-catalyzed graphite felt. Moreover, assuming that the rate of the chemical reactions is much quicker than the species
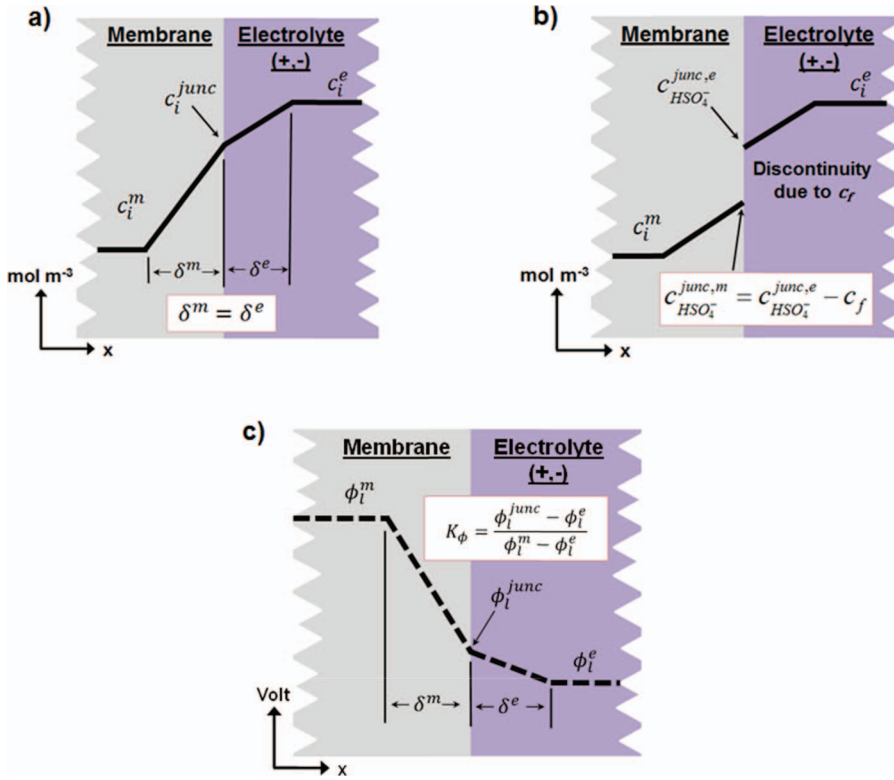

Figure 2. Schematic of the momentum boundary layer at the membrane|electrolyte interface under no-slip conditions for laminar flow. ($\delta_{momentrum} \approx 100 \ \mu m$)

Figure 3. Schematic of the a) generalized species concentration distribution, b) HSO_4^- concentration distribution and c) potential distribution at the electrolyte|membrane interface, which illustrates the concept of an electrolyte and membrane interfacial region. ($\delta^e = \delta^m \approx 1\mu m$)

flux and all side reactions instantaneously occur upon entrance into the electrolyte region, the flux of the vanadium and hydrogen species at the electrolyte interfacial region can be represented by the following boundary conditions:

Negative membrane|electrolyte interface ($x = x_2$, see Fig. 1):

$$-\vec{n} \cdot \vec{N}_{H+}^e = N_{H+}^{er} - 2N_{IV}^{er} - 4N_V^{er} \qquad [31a]$$

$$-\vec{n} \cdot \vec{N}_{II}^e = N_{II}^{er} - N_{IV}^{er} - 2N_V^{er} \qquad [31b]$$

$$-\vec{n} \cdot \vec{N}_{III}^e = N_{III}^{er} + 2N_{IV}^{er} + 3N_V^{er} \qquad [31c]$$

Positive membrane|electrolyte interface ($x = x_3$, see Fig. 1):

$$-\vec{n} \cdot \vec{N}_{H+}^e = N_{H+}^{er} - 2N_{II}^{er} \qquad [32a]$$

$$-\vec{n} \cdot \vec{N}_{IV}^e = N_{IV}^{er} + 3N_{II}^{er} + 2N_{III}^{er} \qquad [32b]$$

$$-\vec{n} \cdot \vec{N}_V^e = N_V^{er} - 2N_{II}^{er} - N_{III}^{er} \qquad [32c]$$

Both interfaces ($x = x_2$ and $x = x_3$, see Fig. 1):

$$-\vec{n} \cdot \vec{N}_{HSO_4^-}^e = N_{HSO_4^-}^{er} \qquad [33]$$

A case study has been performed to compare and validate the concentration and potential jumps predicted at the membrane|electrolyte interface and can be found in Section 3.1.1.

Boundary Conditions.—In the following section, the locations of the boundary conditions are specified in accordance to the x and y coordinates shown in Fig. 1. At the electrode|current collector interface ($x = x_1$ and $x = x_4$) and along the top ($y = h_{cell}$) and bottom ($y = 0$) of the membrane, zero species flux conditions are assumed.

$$0 = \begin{cases} -\vec{n} \cdot \vec{N}_i^e & x = x_2 \text{ and } x = x_3 \\ -\vec{n} \cdot \vec{N}_i^m & y = 0 \text{ and } y = h_{cell} \end{cases} \qquad [34]$$

At the inlets at the bottom of the electrode domains ($y = 0$), the inward flux of the species can be determined from the velocity of the

electrolyte and the concentrations of the species:

$$\left. \begin{aligned} -\vec{n} \cdot \vec{v} &= \frac{\omega}{\varepsilon w_{cell} L_e} \\ c_i^e &= c_i^{in}(t) \end{aligned} \right\} \quad y = 0 \text{ (inlets)} \qquad [35]$$

where w_{cell} is the cell width, L_e is the thickness of the electrode, and ω is the volumetric flow rate. At the outlets at the top of the electrode domains ($y = h_{cell}$), the pressure is set constant, and the diffusion driven flux of the species is assumed to be zero:

$$\left. \begin{aligned} p &= p_{out} \\ -\vec{n} \cdot D_i^{eff} \nabla c_i^e &= 0 \end{aligned} \right\} \quad y = h_{cell} \text{ (outlet)} \qquad [36]$$

At the membrane|electrolyte interface ($x = x_2$ and $x = x_3$, see Fig. 1), the water transfer between the half-cells is incorporated by setting the pressure in the membrane equal to the pressure in the electrode. In addition, the "inlet" velocity into the electrode is taken as equal to the sum of the membrane velocity and the flux of water associated with the crossover side reactions (see Eqs. (29) and (30)):

$$p^m = p^e \quad x = x_2 \text{ and } x = x_3 \qquad [37a]$$

$$-\vec{n} \cdot \vec{v}_j^e = \begin{cases} \vec{n} \cdot \vec{v}^m + \frac{M_w}{\rho_w} \left(N_{IV}^{er} + 2N_V^{er} \right) & x = x_2 \\ \\ \vec{n} \cdot \vec{v}^m + \frac{M_w}{\rho_w} N_{II}^{er} & x = x_3 \end{cases} \qquad [37b]$$

Constant pressure is maintained at the electrode|current collector interfaces in the electrode domain ($x = x_1$ and $x = x_4$, see Fig. 1), which creates a no-slip boundary condition for the velocity:

$$-\vec{n} \cdot \nabla p = 0 \quad x = x_1 \text{ and } x = x_4 \qquad [38]$$

The cell is simulated under constant current density, and the following boundary conditions are applied to the current collectors ($x = 0$ and

$x = x_5$, see Fig. 1) during charging:

$$-\vec{n} \cdot \vec{j}_s^{cc} = \begin{cases} -\dfrac{I}{h_{cell} w_{cell}} & x = 0 \\[2mm] \dfrac{I}{h_{cell} w_{cell}} & x = x_5 \end{cases} \qquad [39]$$

where I is the current, and the signs are reversed during discharging. Consequently, the rest of the cell (top and bottom of the electrode and membrane domains) is taken to be electrically insulated:

$$-\vec{n} \cdot \vec{j}_s^{cc} = -\vec{n} \cdot \vec{j}_s^{e} = -\vec{n} \cdot \vec{j}_l^{m} = -\vec{n} \cdot \vec{j}_l^{e} = 0 \quad y = 0 \text{ and } y = h_{cell} \qquad [40]$$

The solid potential at the '−' current collector boundary is set to zero and is used as a reference potential for the remainder of the cell:

$$\phi_s^{cc} = 0 \qquad x = 0 \qquad [41]$$

Inlet Concentration, Electrolyte Tanks, and Initial Values.—During the operation of a VRFB, the concentrations of the species in the electrolyte tanks and the volumes of the electrolytes are constantly changing due to the electrochemical reactions and species crossover in the cell. To account for the changes in species concentrations, the inlet concentration for each species is simulated using the conservation of mass as follows:

$$\frac{\partial c_i^{in}}{\partial t} = \frac{\varepsilon w_{cell}}{V_j} \left(\int v_j^{out} c_i^{out} dl - \int v_j^{in} c_i^{in} dl \right) \quad c_i^{in}(0) = c_i^0 \quad [42]$$

where V_j is the tank volume of half-cell j. The superscripts *in* and *out* refer to the value at the inlet or outlet of the electrode. Likewise, the changes in electrolyte volume can be calculated using the following differential equation:

$$\frac{\partial V_j}{\partial t} = \varepsilon w_{cell} L_e \left(v_j^{out} - v_j^{in} \right) \quad V_j(0) = V_T^0 \qquad [43]$$

The range of initial tank volumes, V_T^0, used in this study is given in Table VI along with the operating conditions used in the simulations. It is important to note that the total electrolyte volume of each half-cell is taken as the sum of the tank volume (V_T^0) and the volume in the cell, whereas the electrolyte in the pumps and tubes is neglected.

The initial concentrations for the simulations are given in Table VII. The initial concentrations in the electrolytes represent a VRFB at 15% state of charge (SOC), where SOC is defined as follows:

$$\text{Negative Electrolyte}: SOC = \frac{c_{II}}{c_{II} + c_{III}} \qquad [44a]$$

$$\text{Positive Electrolyte}: SOC = \frac{c_V}{c_{IV} + c_V} \qquad [44b]$$

$$\text{Total Cell}: SOC = \frac{c_{II} + c_V}{c_{II} + c_{III} + c_{IV} + c_V} \qquad [44c]$$

The concentrations of the sulfuric acid species (H^+, HSO_4^-, and SO_4^{2-}) in Table VII were determined based on the electrolyte preparation method[24] and the degree of dissociation (β).

Table VI. Operating conditions and parameters.

Symbol	Description	Value
V_T	Electrolyte volume in half-cell tank (mL)	21–56
T	Operating temperature (K)	300
I	Current (A)	0.4–0.5
ω	Inlet volumetric flow rate (mL min^{-1})	20–30
P_{out}	Outlet pressure (kPa)	100

Table VII. Initial species concentrations.

Symbol	Description	Value
c_{II}^0	V(II) initial concentration in negative electrolyte (mol m^{-3})	156
c_{III}^0	V(III) initial concentration in negative electrolyte (mol m^{-3})	884
c_{IV}^0	V(IV) initial concentration in positive electrolyte (mol m^{-3})	884
c_V^0	V(V) initial concentration in positive electrolyte (mol m^{-3})	156
c_{-,H^+}^0	H$^+$ initial concentration in negative electrolyte (mol m^{-3})	4447.5
c_{+,H^+}^0	H$^+$ initial concentration in positive electrolyte (mol m^{-3})	5097.5
$c_{-,HSO_4^-}^0$	HSO$_4^-$ initial concentration in negative electrolyte (mol m^{-3})	2668.5
$c_{+,HSO_4^-}^0$	HSO$_4^-$ initial concentration in positive electrolyte (mol m^{-3})	3058.5
$c_{Vanadium}^{0,m}$	Initial concentration of all vanadium species in membrane (mol m^{-3})	0
$c_{H^+}^{0,m}$	H$^+$ initial concentration in membrane (mol m^{-3})	1990

Numerical Methods.—The system of equations formulated above was solved using COMSOL Multiphysics software and the built-in tertiary current distribution, Darcy's Law, and ODE options. A mesh size of 380 elements was utilized, and the relative tolerance was set to 2.5×10^{-6}.

Experimental

Charge/Discharge Cycling.— To provide data for model validation, performance tests were conducted using a vanadium flow cell with an active surface area of 10 cm^2. The cell contained two composite graphite current collectors and two GFA5 (SGL Carbon Group, Germany) carbon felt electrodes, which were separated by a Nafion 117 membrane. The electrodes were heat-treated at 400 °C for 6 hours in air to functionalize their surface.[34] To pretreat the Nafion, the membrane was submerged in H$_2$O$_2$ for 30 min at 80 °C, then in boiling water for 30 min. Next, it was soaked in 0.5 M H$_2$SO$_4$ at 80 °C for 30 min, and finally cleansed in boiling water.[8] Two peristaltic pumps were used to circulate the '+' and '−' electrolytes between the cell and storage reservoirs, which were continuously purged with nitrogen gas. In the experiment, each half-cell contained 60 mL of electrolyte. The electrolytes were prepared by filling each half-cell with an initial 60 mL solution of 1040 mol m^{-3} VOSO$_4$ (VO^{2+}) in 4000 mol m^{-3} H$_2$SO$_4$ and charging the solutions at 1.7 V to produce '−' and '+' half-cell solutions consisting of V^{3+} and VO$_2^+$, respectively.[35] The '+' half-cell electrolyte was then replaced by 60 mL of the initial solution, resulting in final electrolyte solutions that consist of 1040 mol m^{-3} V^{3+} in 3480 mol m^{-3} H$_2$SO$_4$ in the '−' half-cell and 1040 mol m^{-3} VO^{2+} and 4000 mol m^{-3} H$_2$SO$_4$ in the '+' half-cell.[24]

Charge/discharge testing of the VRFB was performed at a constant current of 0.4 A, and the electrolytes were maintained at a constant flow rate of 30 mL/min. The cell was charged to a maximum potential of 1.7 V and discharged to a minimum potential of 0.8 V. Open circuit measurements were performed after each galvanostatic charge/discharge step in order to determine the SOC of the system.

Electrode Properties.— It is anticipated that the predictions of a VRFB model would be very sensitive to the input parameters used for the transport properties of the porous electrodes (i.e. porosity, specific surface area, and fiber diameter).[22,36,37] Therefore, to further improve the accuracy of the model, the key structural properties (e.g., specific surface area, porosity and pore radius) of GFA5 graphite felt used in the experiments were obtained using a suite of validated
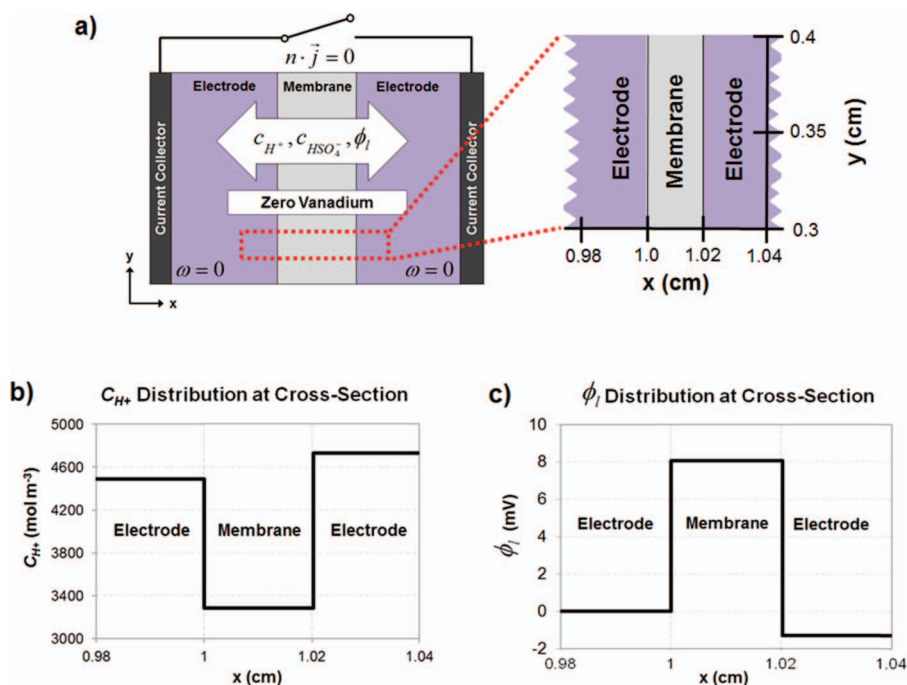
Figure 4. a) Schematic and parameters of simplified model used for interfacial physics validation; b) distribution of hydrogen proton concentration and c) distribution of electrolyte potentials across the membrane (electrode|membrane interfaces occur at x = 1 and x = 1.02 cm). All values in the distributions are taken at the y = 0.35 cm cross-section.

microstructure characterization algorithms described in the authors' previous work.[22,36,37] To summarize, the electrode material was initially imaged using a SkyScan 1172 X-ray tomograph. A binary segmentation was performed on the resulting tomogram to differentiate the solid and pore phases, and then the tomogram was assembled into a 3D virtual volume. A suite of microstructural analysis algorithms were applied to determine the porosity, mean pore diameter, and specific surface area of the material. The porosity was evaluated by discretely counting the number of voxels belonging to the pore phase versus the total number of voxels in the dataset, whereas the surface area was obtained by counting the number of voxel faces occurring at the interface between a pore voxel and a solid voxel. Iterative morphological image operations were used to determine the mean pore diameters. More detailed information regarding the algorithms can be found in.[22,36,37] These properties were used as input parameters for the electrode domain and are presented in Table III.

Results and Discussion

Model Validation.— Membrane|electrolyte Interface.— The first step in the model validation is to determine if the model properly predicts the concentration and potential jumps at the membrane|electrolyte interfaces. Due to the experimental limitations, it is very challenging to obtain in-situ data at these interfaces, which can be used for comparison against the predicted values. Therefore, to validate the interface model, the model predictions were compared against the values predicted by the Donnan potential ($\Delta\phi$), which represents the potential jump at the membrane|electrolyte interface for a system in *equilibrium*. In particular, the potential jump ($\Delta\phi$) and concentrations (c_c^e and c_c^m) at the interface predicted by the model were compared against the values computed by the Donnan potential given in Eq. 45:[38]

$$\Delta\phi = \frac{RT}{F} \ln\left(\frac{c_c^e}{c_c^m}\right) \qquad [45]$$

where the subscript c denotes the cation species.

Equation 45 is valid for a single cation electrolyte which is in *equilibrium* with a semi-permeable membrane (i.e., when no net charge transfer occurs across the membrane|electrolyte interface). However, our present model does not meet these requirements, as it has multiple cations and a net current. Therefore, in order to compare the results

of the mass and charge transport equations (Eq. 24-27) against the Donnan potential, a simplified model that simulates a static flow cell in *equilibrium* was developed based on the formulation outlined in Section 2.1. In this model, the cell was assumed to be static ($\omega = 0$) and there was no reaction current or net current density ($i = j = 0$). All other initial values, parameters, and physics remained the same (Fig. 4a). Using the same numerical methods described in Section 2.1.8, the time dependent problem was solved until $\frac{\partial E_{cell}}{\partial t} \approx 0$, which indicates that the species within the electrolyte reached equilibrium. Figures 4b and 4c depict the predicted distributions of c_{H+} and ϕ_l at the interfacial regions of the membrane during equilibrium. The transition from electrolyte to membrane occurs at x = 1.0 cm ('−' electrode interface) and x = 1.02 cm ('+' electrode interface). To compare the predictions, the c_{H+} values captured from Figure 4b were incorporated into Eq. 45, and the theoretical Donnan potentials were calculated at the two interfaces. When these results were compared to the predicted potential jumps (Fig. 4c), an average error of 0.42% was observed, indicating that the present model can accurately capture the potential and concentration jumps at the membrane|electrolyte interfaces.

Performance and Capacity Loss Validation.— The second step in the model validation is to compare the performance predictions of the model (i.e., voltage and capacity loss) with experimental data. First, a single-cycle was simulated to match the experimental operating conditions described in Section 2.2.1. The simulation was conducted as follows: i) charging was started at an initial SOC of 15%, ii) charging continued until the cell voltage reached 1.7 V, and iii) the cell was discharged until the SOC was 15%. The starting and ending SOC's of the simulation were selected to match the starting and ending experimental SOC data.

Figure 5a shows the comparison between the simulated results and experimental data. A very good agreement in voltage (less than 2% average error) was observed. The authors believe that this accuracy is a result of three main factors: i) the inclusion of the contribution of the hydrogen protons at the '+' electrode in the Nernst equation, ii) the incorporation of additional potential jumps at the membrane|electrolyte interfaces, and iii) the fact that both the '−' and '+' reaction rate constants (k_- and k_+) and charge transfer coefficients (α_- and α_+) were taken as fitted parameters. To the best of the authors' knowledge, the values of k and α have not been reported in the literature for the graphite felt used in the experimental set-up, and the authors are
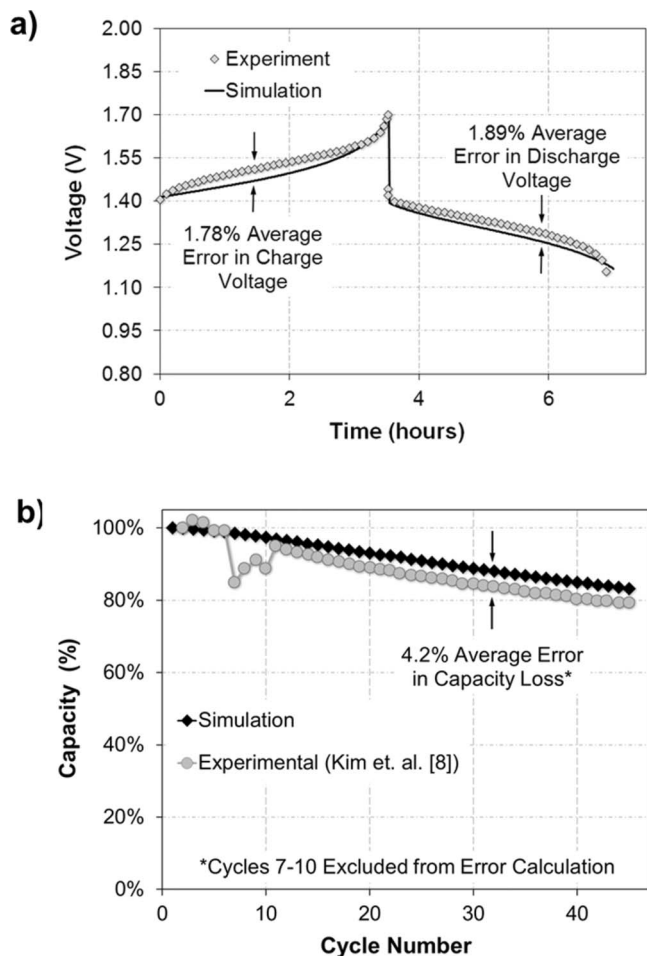
Figure 5. a) Comparison of simulated results with experimental data for a 10 cm^2 VRFB with a half-cell electrolyte volume of 60 mL and a concentration of 1040 mol m^{-3} vanadium and 5000 mol m^{-3} sulfate. The cell was operated at a 30 mL min^{-1} electrolyte flow rate and a 40 mA cm^{-2} constant current density. b) Comparison of the change in cell capacity (discharge time) after 45 cycles between the simulation and experimental data published in[8] for a 10 cm^2 VRFB cell operated at a 20 mL min^{-1} electrolyte flow rate and a 50 mA cm^{-2} constant current density.
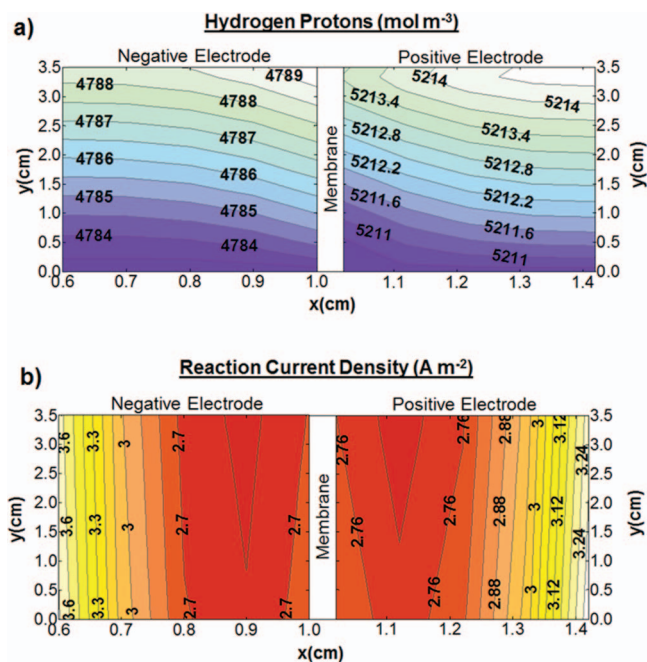

Figure 6. Distributions of a) hydrogen proton concentration and b) magnitude of reaction current density during charging at 50% SOC. Data taken from the single cycle simulation (10 cm^2 cell, 30 mL min^{-1} electrolyte flow rate, and 40 mA cm^{-2} constant current density).

currently working to experimentally determine these values. It is also important to note that along with k and α, the diffusion coefficient of V(II) in the membrane (3.125 × 10^{-12} m^2 s^{-1}) and the electrokinetic permeability (1.13 × 10^{-20} m^2) of the membrane were also taken as fitted parameters due to the lack of data for Nafion 117 in literature, and to match the coulombic efficiency of the experimental data (97%).

A second validation was performed to compare the capacity loss predicted by the model after 45 cycles against experimental data published by Kim et al.[8] The tests in[8] were conducted at the following conditions: 50 mL of electrolyte per half-cell, electrolyte concentrations of 2000 mol m^{-3} vanadium and 5000 mol m^{-3} total sulfate, electrode surface area of 10 cm^2, a constant flow rate of 20 mL min^{-1}, and a constant current of 0.5 A. The model was simulated under similar conditions, however the electrolyte volume and vanadium concentration were reduced to 25 mL and 1040 mol m^{-3}, respectively to reduce the computing time. During the simulation, the cell was charged to a maximum voltage of 1.7 V and discharged to a minimum voltage of 1.1 V, which is equivalent to ∼95% and ∼10% SOC, respectively. The capacity for each simulated cycle was calculated in reference to the discharge time of the first cycle:

$$capacity = \left(\frac{t_{dis,n}}{t_{dis,1}}\right) \times 100\% \qquad [46]$$

where, $t_{dis,n}$ is the discharge time of the nth cycle. A comparison between the simulated results and the experimental data is shown in Fig. 5b. Over the 45 cycles, an average error of 4.2% (consistent throughout the cycles) is observed between the simulated and experimental results. It is anticipated that this slight discrepancy is due to the fact that crossover is the only source of capacity loss in the model. Other factors such as gas evolution, shunt currents, and electrolyte leakage that may affect the capacity loss in the experiments are assumed negligible.

Concentration and Current Distributions in Electrodes.— Once validated, the simulations were performed to assess the model capabilities. Figure 6a depicts the concentration distribution in the '+' and '−' electrodes at 50% SOC during charging of the cell. These results were obtained for the single cycle simulation. The simulation results indicate that both the '+' and '−' electrolytes show an increase in proton concentration along the y-axis. The concentration increase in the '+' electrolyte can be attributed to the redox reaction at the electrode surface, whereas the increase in the '−' electrolyte can be attributed to the transport of hydrogen protons across the membrane (from '+' to '−' electrode) to maintain electroneutrality. In addition, Fig. 6a shows a disparity in concentration between the two half-cells, which is believed to be caused by the electrolyte preparation method.[24]

Figure 6a also shows a slight increase in the proton concentration near the '+' current collector (x = 1.42 cm). It appears that this increase in concentration can be caused by the high reaction current near the current collector (Fig. 6b), which corresponds to a higher production of hydrogen protons. The observed increase of the reactions in the vicinity of the current collectors can be attributed to the fact that the conductivity of the solid electrode (σ_s^e) is lower than the conductivity of the liquid electrolyte (σ_l^{eff}). In other words, the ionic current is expected to be more favorable than the electronic current because the electrolyte region is less resistive than the electrode region. In order to minimize the electronic and maximize the ionic current, a large amount of reactions is expected to occur close to the current collector.

For this simulation, the conductivity of the solid electrode is taken as 66.7 S m^{-1} (reported by manufacturer) and the average effective

a)
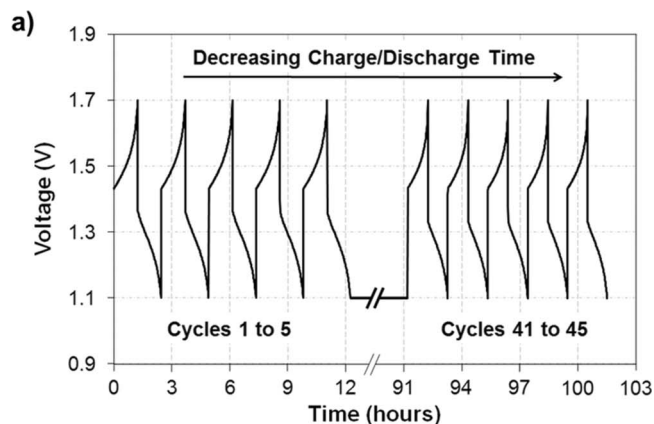
b)

Cycle	Charge Time (seconds)	Discharge Time (seconds)	Capacity (%)
1	4512	4356	100.0%
2	4490	4349	99.8%
3	4479	4341	99.7%
4	4468	4329	99.4%
5	4455	4317	99.1%
⋮	⋮	⋮	⋮
41	3793	3685	84.6%
42	3776	3668	84.2%
43	3761	3653	83.9%
44	3745	3637	83.5%
45	3730	3621	83.1%

Figure 7. a) Charge/discharge performance of cycles 1 to 5 and 41 to 45 for the extended charge/discharge simulation (10 cm^2 cell, 20 mL min^{-1} electrolyte flow rate, and 50 mA cm^{-2} constant current density). b) Tabulated data of the charge/discharge times and percent of initial capacity for the cycles shown in part (a).

Figure 8. a) Efficiencies and b) maximum state of charge (SOC) for the extended charge/discharge simulation (10 cm^2 cell, 20 mL min^{-1} electrolyte flow rate, and 50 mA cm^{-2} constant current density). Maximum SOC was determined at the cutoff voltage of 1.7 V.

conductivity of the electrolyte is 200 S m^{-1} (found from Eq. 23). The low conductivity in the electrode and high conductivity in the electrolyte is most likely due to the high porosity ($\varepsilon = 0.93$) of the carbon felt. The high porosity corresponds to a low quantity of connected fibers (high resistance) for electron transport and a large amount of void space (less resistance) for ion transport. These predictions highlight the importance of analyzing the tradeoffs between electronic and ionic conductivity when designing a high performance electrode material. In addition, it is important to note that the predicted value of the electrolyte conductivity is higher than the reported maximum of sulfuric acid ($\sim$100 S/m[39]). This can be due to the limitation in the ability of the dilute solution approximation to account for the intermolecular interactions occurring in highly concentrated solutions. However, it appears that this issue does not significantly limit the accuracy of the model predictions as shown by the comparison of model predictions with the experimental data.

Simulated Performance for 45 Cycles.— The model was also utilized to investigate the trends in performance over 45 cycles. The voltage curves for the first 5 and last 5 charge/discharge cycles are provided in Fig. 7a, and the charge time, discharge time, and percent capacity loss for each cycle are given in Fig. 7b. Overall, a 16.9% decrease in discharge time is predicted after $\sim$100 hours of operation, which corresponds to a reduction in discharge time from 72.6 to 60.3 minutes. As anticipated, the model results also suggest that the vanadium transport through the membrane significantly reduces the lifetime of a VRFB.

Figure 8a shows the voltage, coulombic, and energy efficiencies for all 45 cycles, which have average values of 83%, 97%, and 80.5%,
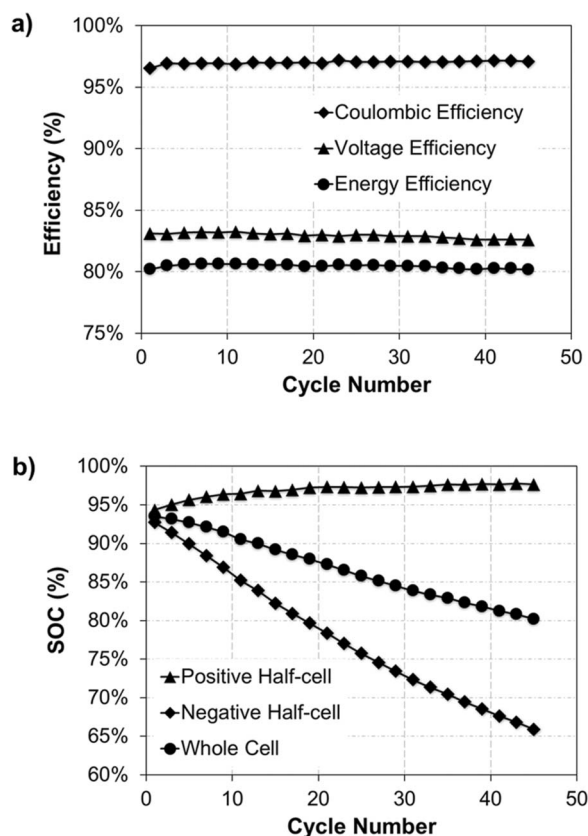
respectively. The simulations show that there is no significant change in the efficiencies after 45 cycles, suggesting that the loss in capacity has a minimal effect on the cell efficiencies. The same behavior was also reported by Kim et al.[8] for 45 experimental charge/discharge cycles. Figure 8b shows the SOC of the '+' half-cell, '−' half-cell, and whole cell at the maximum charging cutoff voltage of 1.7 V for each cycle. From Fig. 8b, it appears that the loss in charge/discharge capacity occurs due to a decrease in the maximum SOC of the whole cell, which indicates that the amount of vanadium reacting during charging is decreasing over time. This behavior suggests that there may be a net transfer of vanadium from one half-cell to the other. To clarify, if one half-cell is becoming depleted and the other enriched with vanadium, the charging time will be limited by the amount of vanadium in the depleted half-cell. All of the vanadium in the depleted half-cell is expected to react during charging, which will cause the cell to reach the cutoff voltage before all the vanadium in the enriched half-cell can react. This will result in the depleted half-cell maintaining a high SOC at the end of charging while the SOC of the enriched half-cell decreases for each cycle.

Based on the simulation results shown in Fig. 8b, it appears that the '+' half-cell has a consistently high SOC (greater than 94%) at the end of charging, while the SOC in the '−' half-cell is steadily declining. This trend suggests that the '+' half-cell SOC is being depleted of vanadium while the '−' half-cell is becoming enriched. In other words, the simulation indicates that a net vanadium transfer from the '+' to '−' half-cell may be responsible for the decrease in the maximum SOC of the cell, and hence, the capacity of the system.

Trends in Vanadium Crossover.—Figure 9a plots the total amount of vanadium in each half-cell (electrode + tank) at the end of each cycle, where cycle "0" represents the initial conditions. As expected from the observed trends in SOC, the simulation indicates a net
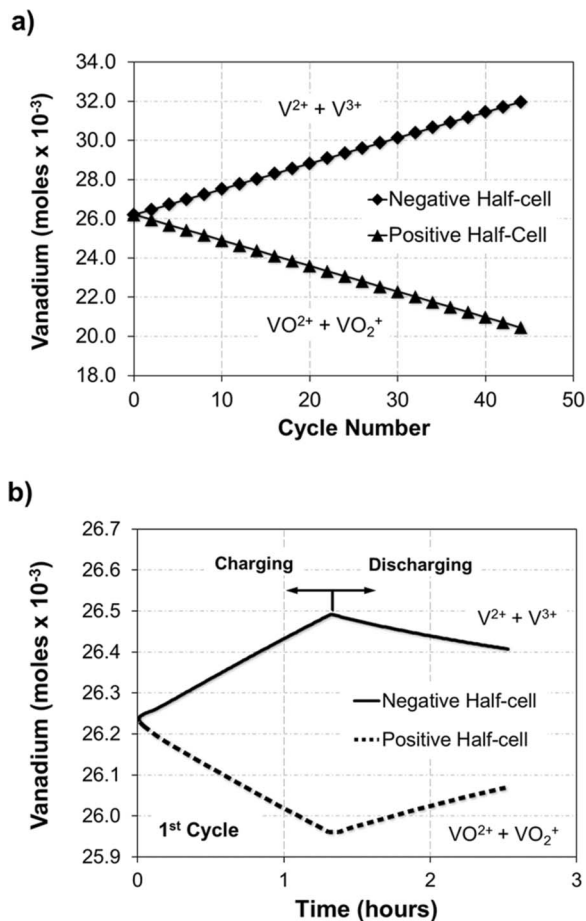
a)

b)

Figure 9. Quantity of vanadium in each half-cell a) at the end of each cycle and b) during the first charge/discharge cycle of the extended simulation (10 cm² cell, 20 mL min⁻¹ electrolyte flow rate, and 50 mA cm⁻² constant current density).

transfer of vanadium from the '+' to '−' half-cell. Previous studies have predicted[20,21] that the net rate of vanadium crossover occurs from the '−' to '+' half-cell due to the higher average diffusion coefficients of V^{2+} and V^{3+} as compared to VO^{2+} and VO_2^+. However, the simulations herein show the opposite trend, which might be due to the fact that diffusion *may not* be the dominating mechanism of species transport in the membrane for *the operating conditions and input parameters tested in this study*. Depending upon the operating conditions (e.g., constant flow rate, constant pressure, etc.), the contribution of convection and migration on the species transport can be more significant as compared to diffusion, which may result in a different trend in vanadium transfer. For instance, a constant flow rate operation can cause pressure gradients across the membrane due to the difference in viscosities of the electrolyte in + and − half cells, which can promote the convective transport of vanadium ions. It is important to note that the predicted trends also depend strongly on *the values used for the electrolyte viscosities*, as they indicate the direction of the pressure drop across the membrane. This suggests that the predicted direction and magnitude of crossover strongly depend on the viscosity of the electrolytes and flow rates used as input parameters in the model. Therefore, along with the membrane properties, the effects of operating conditions and electrolyte properties on the crossover should be carefully analyzed to better understand the mechanisms responsible for the crossover and capacity losses. We are currently performing an in-depth study regarding the role of the operating conditions on the direction and rate of crossover, and the findings of our study will be presented in a separate publication.

Similarly, Fig. 9b shows the total amount of vanadium in each half-cell during the first charge/discharge cycle. According to the simulation, the net vanadium crossover in the cell is always in the same direction as the cell current. During charging, the net vanadium crossover is from the '+' to '−' half-cell and vice versa for discharging. The observed trends are believed to be caused by the contributions of migration and electro-osmotic convection toward the total vanadium flux. Figure 9b also shows that the amount of vanadium in each half-cell remains unbalanced at the end of the cycle, which is due to the fact that the net amount of crossover from the '+' to '−' half-cell *during charging* exceeds the net amount of crossover from the '−' to '+' half-cell *during discharging*. This data also verifies the exchange in total vanadium between the half-cells observed over the 45 cycles.

Species Distributions in the Membrane.—Hydrogen Protons, Bisulfate, and Potential.— The model was also solved to predict the species and potential distribution in the membrane during operation. Figure 10 shows spatial distributions of hydrogen protons, bisulfate ions (HSO_4^-), and potential in the membrane during charging at 50% SOC. This data was taken from the 45th cycle of the extended charge/discharge simulation. The model predictions suggest that significant amounts of sulfuric acid (protons and bisulfate) exist in the membrane, which varies within the membrane. In addition, a small ohmic drop of ∼2.5 mV is predicted across the membrane, indicating a low membrane resistance, which is most likely as a result of the high proton conductivity of Nafion 117.

*Vanadium Concentration and Flux.—*Figure 11 shows the concentration distributions and fluxes of V^{3+} in the membrane at 50% SOC for the 45th cycle of the charge/discharge simulation. The results indicate that convection and migration have significant contributions to the total flux across the membrane. Figure 11d shows that convection and migration account for 29% of the total flux across the membrane during discharging, suggesting that the directions of these two transport mechanisms may be responsible for a significant decrease (∼80%) in the net flux of V^{3+} during charging as compared to discharging. This behavior can be attributed to the fact that convection and migration occur in the same direction as current. For instance, during charging, the net flux is reduced because convection and migration occur in the opposite direction of diffusion. Consequently, during discharging, all three transport mechanisms are in the same direction and a higher rate of crossover is observed.

Figure 12 shows the concentration distributions and fluxes of VO^{2+} in the membrane at 50% SOC. Similar to V^{3+}, Fig. 12 also suggest that convection and migration have a significant impact on the net crossover of VO^{2+}. For instance, Fig 12b shows that these two transport mechanisms account for 44% of the total flux across the membrane during charging. Accordingly, the direction of convection and migration can cause a significant decrease (∼65%) in the net flux of VO^{2+} during discharging as compared to charging. In fact, when analyzed with the trends observed for the V^{3+} flux, this data suggest that during charging, convection and migration cause a net vanadium crossover from the '+' to '−' half-cell and vice versa for discharging. As expected, these trends in flux support the observed changes in vanadium over a single charge/discharge cycle; such that the total amount of vanadium *increases* in the '−' half-cell and *decreases* in the '+' half-cell during charging, and vice versa for discharging.

Conclusions

This study reports a new mathematical framework for a 2-D, transient, isothermal VRFB model which incorporates the transport of all charged species (i.e. vanadium ions, protons, and bisulfate) across the membrane due to convection, diffusion, and migration. The model accounts for the changes in the membrane potential due to the species concentrations and the semi-permselective nature of the membrane, and includes variations in the electrolyte volumes as a result of convection across the membrane. In addition, the model captures the
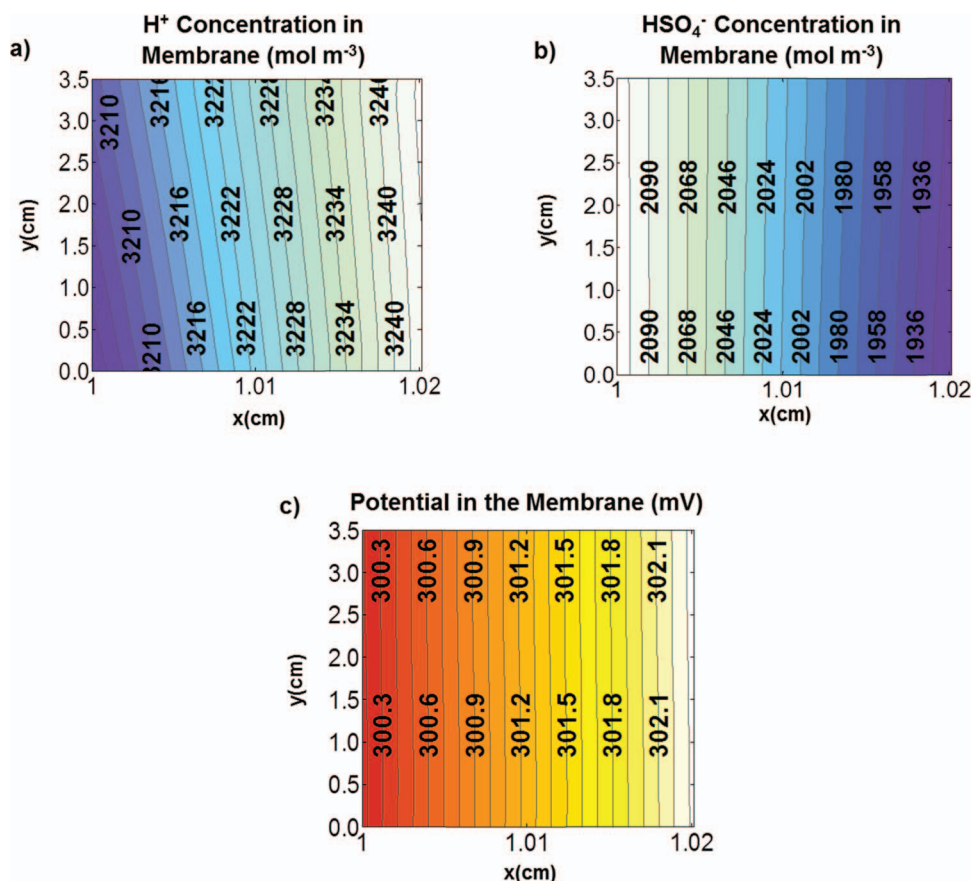
Figure 10. Distributions of a) hydrogen proton concentration, b) bisulfate concentration, and c) potential in the membrane during charging at 50% SOC. Data taken from the 45th cycle of the extended charge/discharge simulation (10 cm^2 cell, 20 mL min^{-1} electrolyte flow rate, and 50 mA cm^{-2} constant current density).
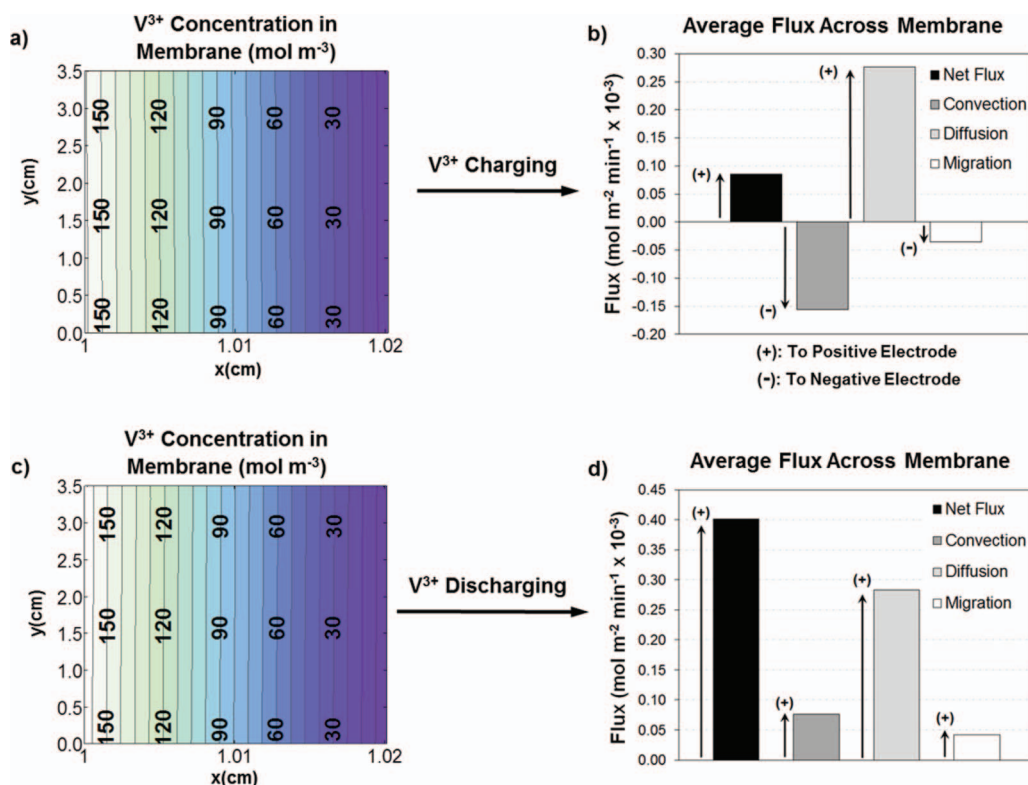

Figure 11. Concentration distributions (a, c) and average fluxes (b, d) of V^{3+} in the membrane during charging (a, b) and discharging (c, d). Data obtained at 50% SOC during the 45th cycle of the extended charge/discharge simulation (10 cm^2 cell, 20 mL min^{-1} electrolyte flow rate, and 50 mA cm^{-2} constant current density).
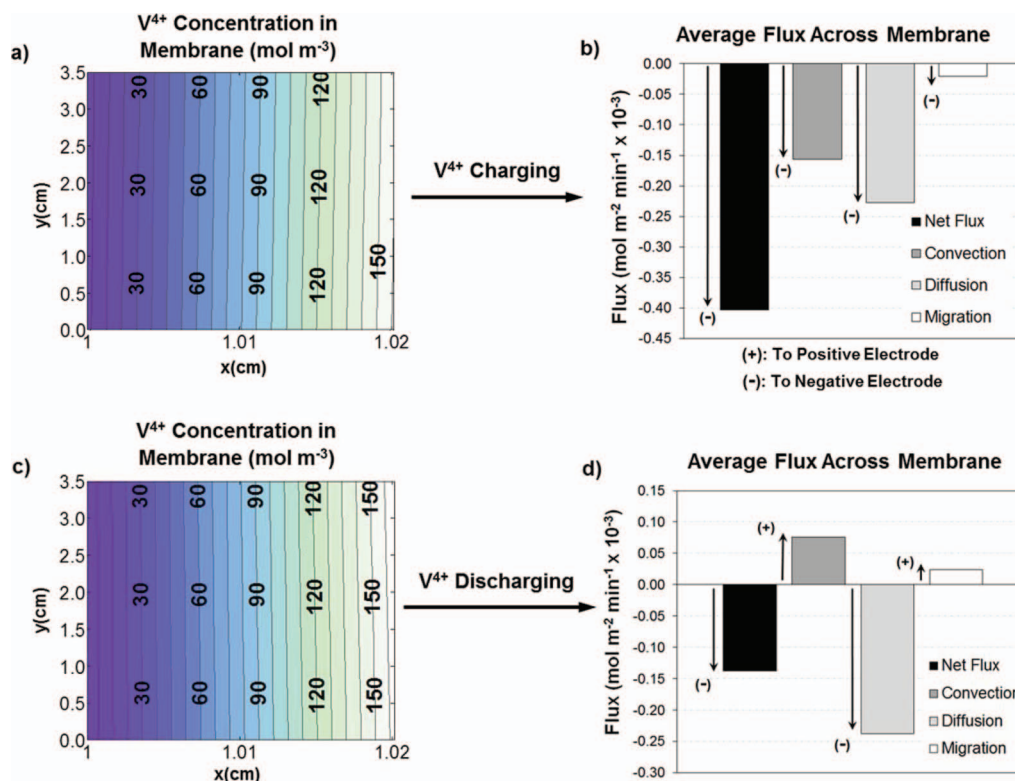
Figure 12. Concentration distributions (a, c) and average fluxes (b, d) of VO^{2+} in the membrane during charging (a, b) and discharging (c, d). Data obtained at 50% SOC during the 45th cycle of the extended charge/discharge simulation (10 cm^2 cell, 20 mL min^{-1} electrolyte flow rate, and 50 mA cm^{-2} constant current density).

discontinuities in the potential and species concentrations at the membrane|electrolyte interfaces and incorporates the effects of side reactions as a result of vanadium crossover.

Based on the input parameters used, the model predictions suggest that the electrode and electrolyte conductivities determine the location of the reactions, and for this study, the majority of the reactions is found to occur in the vicinity of the current collectors due to the lower conductivity of the solid electrode as compared to the liquid electrolyte. The 45 cycle simulations indicate that the loss in capacity may have a minimal effect on the cell efficiencies and that a net transfer of vanadium from the '+' to '−' half-cell is responsible for the loss in capacity. An analysis of the model formulation suggests that the predicted direction and magnitude of crossover are highly dependent on the operating conditions and input parameters (especially, *flow rates* and *viscosities*) used in the simulation. Additionally, the ohmic loss is found to be relatively small across the membrane (~2.5 mV) due to the high proton conductivity of Nafion 117. Finally, the predicted trends of vanadium concentration and flux in the membrane suggest that depending upon the operating conditions, along with diffusion, convection and migration can significantly impact the rate and direction of crossover during VRFB operation.

An in-depth study that includes the analysis of longer cycles, different membrane materials and varying operating conditions is underway to better understand the driving mechanisms responsible for the crossover, capacity loss, and related performance loss (i.e., efficiencies and power output). The findings of our ongoing work will be reported in a separate publication.

List of Symbols

Variables

a	specific surface area (m^2 m^{-3})
c	concentration (mol m^{-3})
C_{KC}	Kozeny-Carmen constant
d_f	fiber diameter (μm)
D	diffusion coefficient
E_0	open circuit voltage
E_0'	standard reduction potential
E	voltage (V)
F	Faraday's Constant
h	height
i	reaction current density
I	current
$\vec{j}$	current density
k	reaction rate/coefficient
K_ϕ	interfacial coefficient
L	component thickness (m)
M	molecular weight (g mol^{-1})
$\vec{n}$	outward normal vector
$\vec{N}$	flux (mol m^{-3} s^{-1})
p	pressure
r_p	pore radius
R	universal gas constant
S	source/sink (mol m^{-3} s^{-1})

t	time
T	temperature (K)
u	ion mobility
$\vec{v}$	velocity (m s^{-1})
V	volume (mL)
w	width
z	valence

Greek

α	transfer coefficient
β	degree of dissociation
δ	region thickness (m)
ε	porosity
η	overpotential (V)
κ	permeability (m^2)
μ	dynamic viscosity
ρ	density (g cm^{-3})
σ	conductivity
ϕ	potential (V)
ω	volumetric flow rate (m^3 s^{-1})

Subscripts

$-$	negative half-cell
$+$	positive half-cell
c	cation
$cell$	property of cell
f	fixed membrane structure
i	species: V^{2+}, V^{3+}, VO^{2+}, VO_2^+ H^+, HSO_4^-, and SO_4^{2-}
j	negative or positive half-cell ($-$ or $+$, respectively)
l	liquid or ionic
s	solid or electronic
T	tank
w	water

Superscripts

0	initial condition
cc	current collector domain
e	electrode or electrolyte domain
eff	effective value
er	interfacial electrode region
in	inlet
$junc$	interfacial junction
m	membrane domain
mr	interfacial membrane region
out	outlet
s	surface

References

1. Z. Yang, J. Zhang, M. Kintner-Meyer, X. Lu, D. Choi, J. P. Lemmon, and J. Liu, *Chem. Rev.*, **111**, 3577 (2011).
2. K. Divya and J. Ostergaard, *Electr. Power Syst. Res.*, **79**, 511 (2009).
3. H. Ibrahim, A. Ilinca, and J. Perron, *Renew. and Sustain. Energy Rev.*, **12**, 1221 (2009).
4. M. Skyllas-Kazacos, M. Chakrabarti, S. Hajimolana, F. Mjalli, and M. Saleem, *J. Electrochem. Soc.*, **158**, R55 (2011).
5. C. Sun, J. Chen, H. Zhang, X. Han, and Q. Luo, *J. Power Sources*, **195**, 890 (2010).
6. D. Chen, S. Wang, M. Xiao, and Y. Meng, *J. Power Sources*, **195**, 2089 (2010).
7. C. Jia, J. Liu, and C. Yan, *J. Power Sources*, **195**, 4380 (2010).
8. S. Kim, J. Yan, B. Schwenzer, J. Zhang, L. Li, J. Liu, Z. Yang, and M. Hickner, *Electrochem. Commun.*, **12**, 1650 (2010).
9. X. Teng, Y. Zhao, J. Xi, Z. Wu, X. Qiu, and L. Chen, *J. Power Sources*, **189**, 1240 (2009).
10. X. Teng, Y. Zhao, J. Xi, Z. Wu, X. Ziu, and L. Chen, *J. Membr. Sci.*, **341**, 149 (2009).
11. M. Li and T. Hikihara, *IEICE Trans. Fundamentals*, **E91-A**, 1741 (2008).
12. A. A. Shah, M. J. Watt-Smith, and F. C. Walsh, *Electrochim. Acta*, **53**, 8087 (2008).
13. H. Al-Fetlawi, A. A. Shah, and F. C. Walsh, *Electrochim. Acta*, **55**, 78 (2009).
14. A. A. Shah, H. Al-Fetlawi, and F. C. Walsh, *Electrochim. Acta*, **55**, 1125 (2010).
15. H. Al-Fetlawi, A. A. Shah, and F. C. Walsh, *Electrochim. Acta*, **55**, 3192 (2010).
16. D. You, H. Zhang, and J. Chen, *Electrochim. Acta*, **54**, 6827 (2009).
17. M. Vynnycky, *Energy*, **36**, 2242 (2011).
18. X. Ma, H. Zhan, and F. Xing, *Electrochim. Acta*, **58**, 238 (2011).
19. A. Tang, J. Bao, and M. Skyllas-Kazacos, *J. Power Sources*, **196**, 10737 (2011).
20. A. Tang, S. Ting, J. Bao, and M. Skyllas-Kazacos, *J. Power Sources*, **203**, 165 (2012).
21. M. Skyllas-Kazacos and L. Goh, *J. Membr. Sci.*, **399**, 43 (2012).
22. G. Qiu, A. Joshi, C. R. Dennison, K. W. Knehr, E. C. Kumbur, and Y. Sun, *Electrochim. Acta*, **64**, 46 (2012).
23. A. Weber, M. Mench, J. Meyers, P. Ross, J. Gostick, and Q. Liu, *J. Appl. Electrochem.*, **41**, 1137 (2011).
24. K. W. Knehr and E. C. Kumbur, *Electrochem. Commun.*, **13**, 342 (2011).
25. K. Kontturi, L. Murtomaki, and J. A. Manzanares, *Ionic Transport Processes in Electrochemistry and Membrane Science*, Oxford University Press, New York (2008).
26. D. A. Knopf, B. P. Luo, U. K. Krieger, and T. Koop, *J. Phys. Chem.*, **107**, 4322 (2003).
27. M. Verbrugge and R. Hill, *J. Electrochem. Soc.*, **137**, 886 (1990).
28. P. Xu and B. Yu, *Adv. Water Resour.*, **31**, 74 (2008).
29. C. Blanc, *Modeling of a vanadium redox flow battery electricity storage system*, PhD thesis, EPFL, Switzerland (2009).
30. G. Pourcelly, A. Lindheimer, and C. Gavach, *J. Electroanal. Chem.*, **305**, 97 (1991).
31. J. Newman and K. E. Thomas-Alyea, *Electrochemical Systems*, 3rd ed., John Wiley & Sons, Inc., Hoboken, New Jersey (2004).
32. V. S. Bagotsky, *Fundamentals of Electrochemistry*, 2nd ed. John Wiley & Sons, Inc., Hoboken, New Jersey (2006).
33. K. Vafai and C. Tien, *Int. J. Heat Mass Transfer*, **24**, 195 (1981).
34. S. Zhong, C. Padeste, M. Kazacos, and M. Skyllas-Kazacos, *J. Power Sources*, **46**, 29 (1993).
35. G. Hwang and H. Ohya, *J. Membr. Sci.*, **120**, 55 (1996).
36. E. A. Wargo, A. C. Hanna, A. Cecen, S. R. Kalidindi, and E. C. Kumbur, *J. Power Sources*, **197**, 168 (2012).
37. A. Cecen, E. A. Wargo, A. C. Hanna, S. R. Kalidindi, and E. C. Kumbur, *J. Electrochem. Soc.*, **159**, B1 (2012).
38. C. Hamann, A. Hamnett, and W. Vielstich, *Electrochemistry*, 2nd ed., Wiley-VCH, Germany (2007).
39. H. Darling, *J. Chem. and Engr. Data*, **9**, 421 (1964).
40. G. Oriji, Y. Katayama, and T. Miura, *Electrochim. Acta*, **46**, 3091 (2004).
41. B. Munson, D. Young, T. Okiishi, and W. Huebsch, *Fundamentals of Fluid Mechanics*, 6th ed., John Wiley & Sons, Inc., Hoboken, New Jersey (2009).
42. T. Yamamura, N. Watanabe, T. Yano, and Y. Shiokawa, *J. Electrochem. Soc.*, **152**, A830 (2005).
43. DuPont. website: http://www2.dupont.com/FuelCells/en_US/products/literature.html (accessed 21-6-2011).
44. D. Bernardi and M. Verbrugge, *AIChE J.*, **37**, 1151 (1991).
45. J. Xi, Z. Wu, X. Teng, Y. Zhao, L. Chen, and X. Qiu, *J. Mater. Chem.*, **18**, 1232 (2008).
46. M. Verbrugge, *J. Electrochem. Soc.*, **137**, 893 (1990).